Earth and Planetary Science Letters 534 (2020) 116108

Contents lists available at ScienceDirect

Earth and Planetary Science Letters

www.elsevier.com/locate/epsl

No FeS layer in Mercury? Evidence from Ti/Al measured by MESSENGER

C. Cartier [a,b,c,*], O. Namur [d], L.R. Nittler [e], S.Z. Weider [e], E. Crapster-Pregont [f], A. Vorburger [f], E.A. Frank [e], B. Charlier [a]

[a] Département de Géologie, Université de Liège, 4000, Sart Tilman, Belgium
[b] Laboratoire Magmas et Volcans, Université Blaise Pascal, Clermont-Ferrand, 63038, France
[c] CRPG, CNRS, Université de Lorraine, UMR 7358, Vandoeuvre-lès-Nancy, 54501, France
[d] Department of Earth and Environmental Sciences, KU Leuven, Leuven, 3001, Belgium
[e] Carnegie Institution of Washington, Department of Terrestrial Magnetism, Washington, DC 20015, USA
[f] Department of Earth and Planetary Sciences, American Museum of Natural History, New York, NY 10024, USA

ARTICLE INFO

Article history:
Received 15 May 2019
Received in revised form 11 January 2020
Accepted 17 January 2020
Available online 27 January 2020
Editor: F. Moynier

Keywords:
titanium
core formation
reducing conditions
sulfide matte
magma ocean

ABSTRACT

In this study we investigate the likeliness of the existence of an iron sulfide layer (FeS matte) at the core-mantle boundary (CMB) of Mercury by comparing new chemical surface data obtained by the X-ray Spectrometer onboard the MESSENGER spacecraft with geochemical models supported by high-pressure experiments under reducing conditions. We present a new data set consisting of 233 Ti/Si measurements, which combined with Al/Si data show that Mercury's surface has a slightly subchondritic Ti/Al ratio of 0.035 ± 0.008. Multiphase equilibria experiments show that at the conditions of Mercury's core formation, Ti is chalcophile but not siderophile, making Ti a useful tracer of sulfide melt formation. We parameterize and use our partitioning data in a model to calculate the relative depletion of Ti in the bulk silicate fraction of Mercury as a function of a putative FeS layer thickness. By comparing the model results and surface elemental data we show that Mercury most likely does not have a FeS layer, and in case it would have one, it would only be a few kilometers thick (<13 km). We also show that Mercury's metallic Fe(Si) core cannot contain more than ∼1.5 wt.% sulfur and that the formation of this core under reducing conditions is responsible for the slightly subchondritic Ti/Al ratio of Mercury's surface.
© 2020 Elsevier B.V. All rights reserved.

1. Introduction

Mercury is a peculiar planet because it has a high average density compared to its size, indicating a very large metallic core (∼3/4 of the planet's radius, Anderson et al., 1987). In recent years, geophysical and geochemical measurements by NASA's MESSENGER spacecraft have refined our understanding of the internal structure and geological history of Mercury. Recent libration and gravity field data constrain Mercury's core to be largely liquid and to contain light elements alloyed with iron (Dumberry and Rivoldini, 2015; Genova et al., 2019; Knibbe and Westrenen, 2016; Margot et al., 2018; Rivoldini and Van Hoolst, 2013). The silicate portion of Mercury, comprising a thin mantle and a secondary volcanic crust, also contrasts with other terrestrial bodies. In particular, measurements of low iron (Fe) and exceptionally high sulfur (S) contents in lavas support the idea of a highly reduced planet (Cartier and Wood, 2019; Evans et al., 2012; Malavergne et al., 2010; McCubbin et al., 2012; Namur et al., 2016a; Nittler et al., 2011; Zolotov et al., 2013). Finally, the detection of high concentrations of moderately volatile elements such as potassium, sodium, carbon and chlorine at the surface of Mercury (Peplowski et al., 2011; 2016) challenges some classical models of solar system formation that predict that the innermost planet should be the most depleted in these elements.

Based on MESSENGER chemical maps, particularly for sulfur, and experiments in reduced conditions, the intrinsic oxygen fugacity $\log(fO_2)$ of Mercury's mantle has been estimated to be in the range of IW-6.3 to IW-2.6, with a mean value of IW-5.4 ± 0.4, with IW being the iron-wüstite redox equilibrium (McCubbin et al., 2012; Namur et al., 2016a; Zolotov et al., 2013). Experiments on metal-silicate-sulfide equilibria conducted at these highly reducing conditions suggest the dissolution of important amounts of silicon (Si) in the Fe alloy (Kilburn and Wood, 1997) during core formation. However at 4–7 GPa, which is the estimated pressure of Mercury's CMB, there is a miscibility gap in the Fe-Si-S

* Corresponding author.
E-mail address: camille.cartier@univ-lorraine.fr (C. Cartier).

https://doi.org/10.1016/j.epsl.2020.116108
0012-821X/© 2020 Elsevier B.V. All rights reserved.

system causing the co-existence of two Fe-rich melts: a FeS dominated sulfide melt and an Fe(Si) metallic melt (Morard and Katsura, 2010). In the case of Mercury, if the bulk sulfur content of the planet was high enough, a sulfide melt could have existed in addition to the metallic melts during its early differentiation and merged to form a buoyant layer at the top of the metal silicon-rich core (Chabot et al., 2014; Charlier and Namur, 2019; Malavergne et al., 2010; Namur et al., 2016b). Experimental data as well as geophysics both suggest the potential existence of such an external sulfide layer (solid or liquid), the thickness of which is estimated to be lower than 200 km but is highly dependent on the S content of Mercury's building blocks (Chabot et al., 2014; Malavergne et al., 2010; Smith et al., 2012). This model would be consistent with the hypothesis of a dense and solid layer overlying the dynamo-generating region of the core (Anderson et al., 2012; Hauck et al., 2013; Smith et al., 2012).

Taking the assumption of a bulk Mercury containing 3–5 wt.% sulfur, which corresponds to the range of S contents observed in most chondrites (Lodders and Fegley, 1998), and considering its partitioning between the different shells of the planet during core formation (Boujibar et al., 2014), the FeS layer was calculated to have a likely thickness of 0 to 90 km (Namur et al., 2016a). This is however a maximum estimate because some chondrites (such as CB or CH) contain less than 1 wt.% S. Thus, Malavergne et al. (2010) estimated a FeS thickness between 5 and 15 km if Mercury is made of CB-like material. At last terrestrial planets are expected to be more depleted in volatile elements (including sulfur) than chondrites (Albarède, 2009).

In this study we constrain the existence or absence of such a sulfide layer at the CMB, independently of any assumption on the bulk sulfur concentration of the planet. We compare chemical compositions of lavas obtained by the MESSENGER spacecraft (Nittler et al., 2011; Weider et al., 2014, this study) with geochemical models of planetary early differentiation. We use a chalcophile element as a tracer for the potential formation of a sulfide layer because the extraction of a sulfide melt during core merging would have depleted the silicate portion of Mercury in this element (Rubie et al., 2016). A recent experimental study shows that titanium (Ti), which is usually classified as a lithophile element, is chalcophile at the redox conditions of Mercury's mantle (Vander Kaaden and McCubbin, 2016). In the following we: a) present new Ti/Si data measured by MESSENGER at the surface of Mercury, b) present multiphase equilibria experiments that we use to parameterize the geochemical behavior of Ti in Mercurian conditions, c) use partitioning data in a core formation model to calculate the relative depletion of Ti in the bulk silicate Mercury (BSM) as a function of the thickness of the sulfide layer (0–150 km), and d) compare the model results with MESSENGER data to infer the most likely thickness of the sulfide layer.

The potential formation of a FeS layer in Mercury can be compared to the inferred 'Hadean FeS matte' proposed for Earth (O'Neill, 1991; Rubie et al., 2016; Savage et al., 2015). For Mercury it is of particular importance for the thermal history of the planet because the FeS layer would behave as an insulating liquid outermost core (Manthilake et al., 2019; Pommier et al., 2019) and because it could have trapped heat-producing elements such as U and Th, which could change their behavior from lithophile to chalcophile under highly reducing conditions (Boujibar et al., 2019; Cartier and Wood, 2019; McCubbin et al., 2012; Wohlers and Wood, 2017; 2015). Mercury has a significant global magnetic field that can be explained by the dynamo theory if part of the core is still liquid. However, the mineralogy of Mercury's lavas and the conditions of melting in their mantle sources indicate that the secondary volcanic crust formed during very intense episodes of magmatism that ended ∼3.5 Ga ago (Byrne et al., 2016; Marchi et al., 2015; Namur and Charlier, 2017), attesting to a fast secular cooling of the mantle (Namur et al., 2016b). Whether or not heat-producing elements were concentrated in a sulfide layer at the interface between the metal core and the silicate mantle is therefore of great importance to unravel the thermal evolution of Mercury's lower mantle (Tosi et al., 2013). In addition, K/U and K/Th ratios measured at planetary surfaces are often used as proxies for the volatile inventory of terrestrial planets (Lodders and Fegley, 1998; Peplowski et al., 2011; Taylor et al., 2006). However if Th and U were extracted into a sulfide layer during core formation, Mercury surface ratios could have been fractionated from the bulk planet and not be such a reliable proxy for the volatile budget of the planet (McCubbin et al., 2012).

2. Titanium on Mercury

The X-Ray Spectrometer (XRS) on the MESSENGER spacecraft was used to map Mercury's surface composition in a number of geochemically important elements (Nittler et al., 2018; 2011; Weider et al., 2015; 2014; 2012). The XRS detected fluorescent emissions, induced by X-rays emitted from the Sun's corona, from the top tens of micrometers of the planetary regolith. Under typical solar conditions, only the light elements Mg, Al, and Si were detected, but during solar flares, the coronal X-ray flux can increase by many orders of magnitude, causing detectable fluorescence of heavier and/or less abundant elements, including S, Ca, Ti, Cr, and Fe. The spatial resolution of XRS measurements varied widely, owing to the highly elliptical polar orbit of MESSENGER about Mercury, with the best resolution (<100 km) achieved in high northern latitudes, and much poorer resolution in the southern hemisphere. Moreover, the orbit led to much more observing time over the southern hemisphere, so spatial coverage for the flare-dependent heavier elements is incomplete in the northern hemisphere where spatial resolution is best (e.g., Weider et al., 2015). Finally, XRS data are usually reported as elemental ratios to Si since using ratios eliminates many systematic uncertainties and Si is a major element with relatively little overall variation across Mercury (Peplowski et al., 2012).

Because of the need for large flares to detect Ti and its low abundance (<1 wt.%), Ti data have been previously reported for only 25 flares (Nittler et al., 2011; Weider et al., 2014). The relatively poor energy resolution of the XRS gas-proportional counter detectors results in Ti appearing in XRS spectra only as a high-energy shoulder on the Ca peak (see Fig. S6 of Nittler et al., 2011), but this shoulder can be well-fitted by the least-squares methodology used to extract abundances from XRS data (Nittler et al., 2011), provided the signal is high enough. More than 2000 individual flare XRS spectra acquired from throughout the entire 2011-2015 MESSENGER orbital mission were previously fit to extract elemental abundances and generate chemical maps of Mercury's surface (Nittler et al., 2018; 2016; Weider et al., 2015). Of these analyses, 672 had non-zero Ti detections. We used a number of criteria to identify the most reliable Ti measurements from this data set. First, we found very large scatter in measured Ti/Si ratios for solar coronal plasma temperatures (determined from the XRS solar monitor spectra, see Nittler et al., 2011) below 15 MK, so all results for lower temperatures were excluded. Second, flares found to have unusually high detector backgrounds at high energy were excluded, since such backgrounds could significantly affect results for low-abundance elements like Ti. Third, the major-element (Mg/Si, Al/Si, S/Si, and Ca/Si) results for each remaining flare analysis were compared with those in the global maps of these elements for the same area of the surface. Results that strongly diverged from the global maps, which are based on multiple overlapping measurements and hence are considered to be more accurate than individual analyses, for one or more element ratio were excluded. Finally, a few measurements were excluded because they had derived Ti/Si

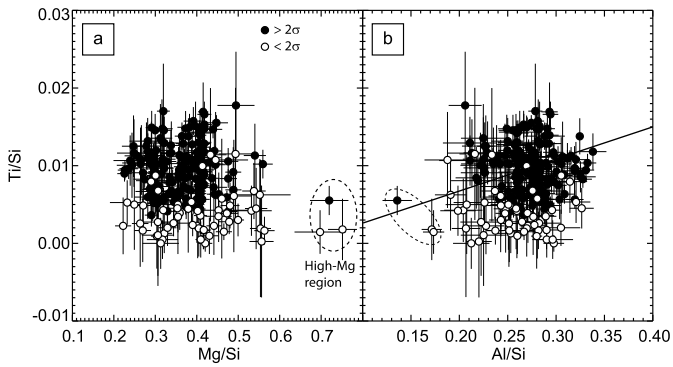

Fig. 1. MESSENGER X-ray Spectrometer measurements of 233 locations on Mercury's surface, ranging in size from 50 to >3000 km. Ti/Si weight ratios are derived from measurements during solar flares and are divided into those with values resolved from 0 (filled circles) and those within 2-sigma of 0 (open circles). Mg/Si and Ti/Si weight ratios are taken from global maps (Nittler et al., 2018) for the same regions sampled by the Ti/Si analyses and represent averages of multiple measurements. The dashed ellipses indicate three measurements from Mercury's high-Mg region (Weider et al., 2015) and the solid line in b) corresponds to the average surface Ti/Al ratio of 0.0345. Error bars are one sigma.

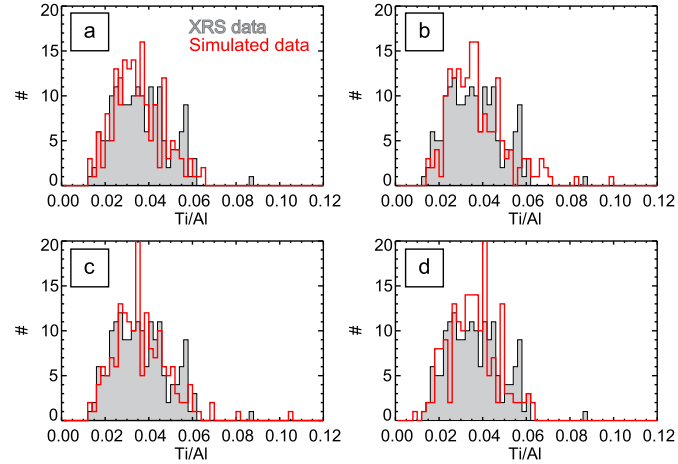

Fig. 2. Histograms of Ti/Al ratios measured on Mercury (gray) compared to four example (a), (b), (c) and (d) simulated datasets (red) with model parameters that best match the observed data, $r = 0.0345$ and $\sigma_{syst} = 0.008$. Only data with Ti/Si resolved from zero by more than two standard deviations are included in both simulated and observed histograms. (For interpretation of the colors in the figure(s), the reader is referred to the web version of this article.)

ratios much higher than other measurements with overlapping footprints. The final data set consists of 233 Ti/Si measurements from across Mercury's surface, provided in the supplementary Table S1.

The 233 measured Ti/Si ratios are plotted against Mg/Si and Al/Si ratios in Fig. 1. The Mg/Si and Al/Si ratios for these points are taken from the global maps (Nittler et al., 2016; Weider et al., 2015) for the XRS footprints corresponding to the Ti measurements. Taking a simple average over the full Ti/Si data set, we obtain a value of 0.0083 with a standard deviation of 0.0040. However, the overall low Ti abundance and relatively large error bars for many data points is likely to lead to biases when calculating averages and any calculated average value will depend strongly on which specific data points are included in the calculation. For example, 57 analyses have Ti/Si ratios that lie within 2σ of zero (open symbols of Fig. 1). As such, they should be considered upper limits and combining them with resolved measurements as we did above to calculate an overall average value is not mathematically justified. Excluding them gives an average Ti/Si ratio for the remaining data set of 0.0098 ± 0.0030, but this is clearly biased towards higher ratios as these are more likely to be resolved from zero. Below we use a Monte Carlo simulation method to more accurately estimate the average Mercury Ti surface abundance and its uncertainty from all 233 measurements. Note that a relatively constant Ti/Al ratio across Mercury's surface is supported by the fact that the three measurements from within the so-called high-Mg region (Frank et al., 2017; Weider et al., 2015), which also has the lowest Al/Si ratios on the planet, all have low Ti/Si ratios (dashed ellipses in Fig. 1).

Accurate estimates of the average Mercury Ti/Al ratio and its error are needed to compare with the results of geochemical models (see Section 5). As discussed above, however, simply averaging the measurements is problematical: combining analyses that are at or below the detection limit with bona fide detections is not straightforward, but excluding them will bias the average towards relatively high values. Averaging all 233 measurements gives Ti/Al $= 0.031$, whereas excluding those data with Ti abundances within 2σ of 0 gives an average value of 0.038 for this ratio. The true surface value undoubtedly lies between these two values. The spread in the data reflects both statistical errors and any additional systematic uncertainty introduced by the XRS technique. To better estimate the true surface Ti/Al ratio and its error, we took a Monte Carlo approach and generated simulated data to compare with the observations. Each simulated "measurement" was drawn randomly from a parent probability distribution, assumed to be Gaussian with mean value r and standard deviation σ_{syst}. The parameter r represents the true surface Ti/Al ratio and σ_{syst} the assumed intrinsic systematic uncertainty for the XRS method, i.e., the limiting uncertainty with which we can determine Ti/Al from the data. Each draw, r', from the parent distribution was further assigned a statistical uncertainty, taken randomly from the actual XRS flare measurement uncertainties, and the final simulated data point was drawn from a Poisson distribution based on r' and the corresponding statistical uncertainty. Once a simulated dataset of 233 points was generated for given values of r and σ_{syst}, the average and standard deviation of the resulting Ti/Al data points were calculated and compared to the observed data. In both simulated and observed datasets, only data that differ from zero by more than 2σ were included in this comparison. This process was repeated 100 times each for a range of values of r and σ_{syst}. The best match to the observed data was found for $r = 0.0345$ and $\sigma_{syst} = 0.008$ (Fig. 2); we take these values to be the best estimate of the true Ti/Al ratio of Mercury's surface and its uncertainty. The solid line in Fig. 1(b) indicates the correlation line between Ti/Si and Al/Si corresponding to this value of Ti/Al.

3. Titanium behavior at the conditions of Mercury's core formation

Vander Kaaden and McCubbin (2016) have shown that Ti, which is usually classified as a lithophile element, is chalcophile at the redox conditions of Mercury's mantle. As it is also a highly refractory element, Ti is a very interesting candidate to trace sulfide melt formation during Mercury's early differentiation. In order to get Ti partitioning data relevant for the conditions of Mercury's core formation that can be used in geochemical models, we have conducted equilibrium experiments, mainly at 5 GPa (the likely pressure of Mercury CMB, Hauck et al., 2013), 1520–1850 °C which are sub-liquidus (but super-solidus) to super-liquidus temperatures for chondritic material at this pressure (Andrault et al., 2011), and under a wide range of redox conditions going from moderately reducing (IW-1) to extremely reducing (IW-8) (Table 1).

3.1. Experimental methods and results

Starting material consisted of natural or synthetic enstatite chondrite analogue ground together with various amounts of

Table 1
Experimental conditions and Ti partition coefficients. MA = multi-anvil apparatus; PC = piston cylinder; C = graphite. Pressure in GPa, temperature in K, fO_2 expressed relative to the iron-wüstite equilibrium (IW), fS_2 expressed relative to the iron-troïlite equilibrium (IT) (see text for detail). D are Ti Nernst partition coefficients between sulfide/silicate and metal/silicate, and σ their associated uncertainties.

Run	Device	Caps	P (Gpa)	T (K)	Duration (h)	ΔIW	ΔIT	D(Ti) Sul/sil	σ	D(Ti) Met/sil	σ
1093b	MA	C	5	1953	4	−6	1.0	9.91	5.21	0.12	0.13
1133	MA	C	5	1963	3.5	−5.7	1.0	8.77	6.76	0.17	0.27
1135	MA	C	5	1923	2.5	−6.2	0.8	12.60	10.74	–	–
1136	MA	C	5	1913	2	−5.5	0.9	4.45	3.42	0.09	0.08
1136b	MA	C	5	1913	2	−5.5	0.5	8.78	6.34	0.12	0.10
1137	MA	C	5	1973	3	−2.4	0.5	0.06	0.06	0.02	0.03
1183	MA	C	5	1993	2.3	−2.2	0.3	0.04	0.06	0.05	0.05
1198	MA	C	5	2073	3	−1.4	0.3	0.01	0.02	0.05	0.04
1207	MA	C	5	2073	3	−4.5	0.4	3.09	2.77	0.06	0.10
1210	MA	C	5	2073	2	−5.1	0.6	9.27	11.29	0.35	0.71
1211	MA	C	5	2123	2	−4.3	0.5	5.16	3.47	0.18	0.21
1212	MA	C	5	2123	3	−4.9	0.7	4.12	2.16	0.11	0.15
1143	MA	C	5	1873	3	−7.4	–	–	–	1.24	0.32
1165	MA	C	5	1873	1	−7.8	–	–	–	1.77	3.08
1178	MA	C	5	1853	2	−7.8	–	–	–	2.13	1.50
1184	MA	C	5	1913	2	−7.9	–	–	–	4.61	3.85
B880	PC	C	3	1973	3.5	−5.5	–	–	–	0.42	0.04

metallic Si powder (0–50 wt.%) in order to vary the sample fO_2. The compositional range defined by our starting compositions matches the expected composition of Mercury's magma ocean (Brown and Elkins-Tanton, 2009; Nittler et al., 2018). The bulk chemical composition of our starting powders are given in the supplementary Table S2. Most experiments were performed at 5 GPa in the multianvil press at the Laboratoire Magmas et Volcans (LMV; Clermont-Ferrand, France) with 18/11 and 14/8 assemblies. We used Cr-doped MgO octahedra as pressure transmitting medium, stepped $LaCrO_3$ furnaces and ZrO_2 insulating sleeves. Temperature was monitored using $W_5Re_{95}/W_{26}Re_{74}$ type C thermocouples, with no correction for pressure effect on the electromotive force. In case of thermocouple loss, temperature was determined from power/temperature relations determined in previous experiments. In addition, one experiment was run at 3 GPa in a 0.5″ piston cylinder at University of Bayreuth (Germany). The powders were loaded in graphite capsules and samples were heated to temperatures ranging between 1520 and 1850 °C. Capsule length was 2 mm resulting in a temperature gradient of less than 50° in the investigated range (Hammouda et al., 2010). Run duration at high temperature ranged between 2 and 8 h, which is sufficient to reach equilibrium at these pressure-temperature conditions (Cartier et al., 2014b). Indeed, all the samples selected for this study show equilibrium textures (see below) and all phases are chemically homogeneous within a sample. Samples were quenched by switching off the electrical power resulting in quench rates of several hundreds of degrees per second. Experimental conditions are given in Table 1.

Recovered charges were mounted in epoxy and subsequently polished with alcohol-based suspensions and lubricants. Phase identification was performed with a scanning electron microscope (JEOL JSM-5910LV) which we also used to acquire back-scattered electron images. Most charges consist of three main equilibrated phases: silicate glass, metallic melt forming big blebs surrounded by immiscible sulfide melts of almost stoichiometric FeS composition (Fig. 3). Many charges also contain crystals (enstatite and coesite) which, where present, are euhedral (Fig. 3). Phase proportions are given in the supplementary Table S3. On average our samples contain 30% silicate melt, 37% enstatite, 25% metallic melt, 4% sulfide melt and 3% coesite. Some of these experiments have been presented in Cartier et al. (2014a; 2014b), but here we report for the first time chemical compositions of the sulfide phase.

Most silicate melts are perfectly quenched, as shown on Fig. 3. On the contrary, metal and sulfide melts display a diversity of quench textures consisting of emulsion of microdroplets of two or three different compositions, exsolved from the melt during the quench. These textures are the same as those described in detail by Morard and Katsura (2010) and typical of quenched multicomponent alloys.

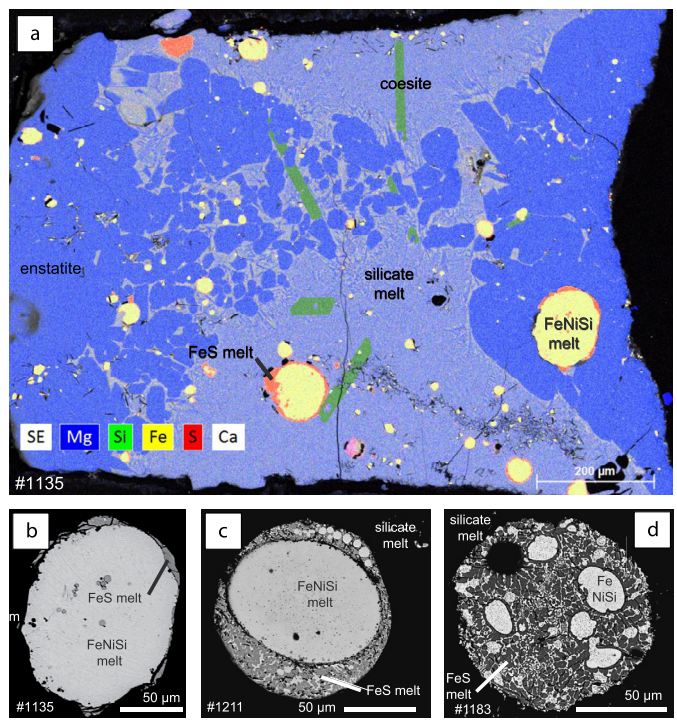

Fig. 3. EDS chemical maps (a) and BSE images (b), (c), (d) of experimental samples. (a) Sample 1135 is a typical run product. It contains 17% silicate melt, 46% enstatite, 29% FeNiSi melt, 5% FeS melt and 3% coesite. Enstatite and coesite crystals are euhedral. FeS melt almost always surround FeNiS beads (BSE), forming typical metal-sulfide associations. (b), (c), (d) Detail of metal-sulfide in samples 1135, 1211 and 1183. FeNiSi and FeS melts show typical quench textures consisting in an emulsion of various composition droplets (Morard and Katsura, 2010).

3.2. Experimental sample analysis

Quantitative analyses of major and minor elements in each phasis were obtained with an electron microprobe CAMECA SX100 at LMV and the University of Hannover (LUH), operated with an accelerating voltage of 15 kV and beam currents of 15 nA for metal

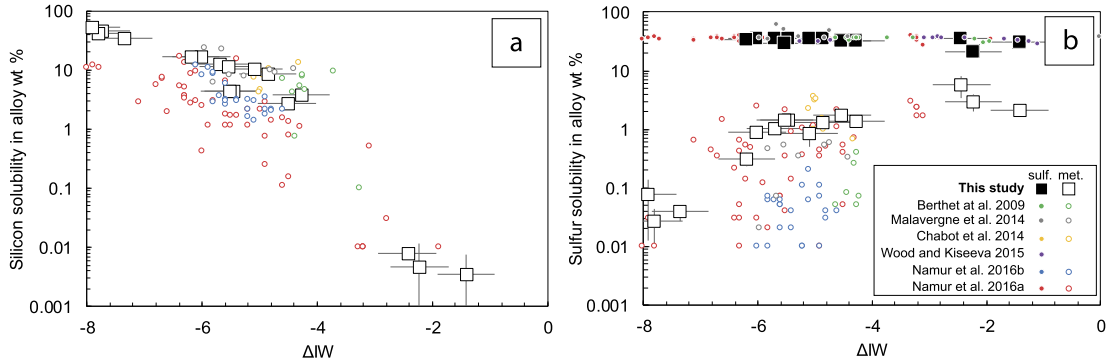

Fig. 4. Silicon (a) and sulfur (b) contents at sulfide saturation in Fe-rich alloys as a function of oxygen fugacity (ΔIW). Our experiments were performed at 5 GPa (except one experiment which was conducted at 3 GPa), at near liquidus temperatures, and are saturated with an FeS sulfide liquid. Error bars correspond to ±1 sigma uncertainties on Ti data and fO_2 estimates. Literature data correspond to experiments conducted between 1 bar and 4 GPa, at various temperatures, and in FeS saturated systems.

and sulfide melts and 4–8 nA for silicate glasses. In order to avoid sampling bias due to quench textures (in particular in metal and sulfide phases, Fig. 3), the beam was defocused according to the size of each phase. Oxygen concentrations of most glasses were measured with the electron microprobe using a PC1 crystal with counting time of 15 s on peak. The standards were natural minerals and synthetic oxides for silicates (Si, Ca: wollastonite; Mg: Forsterite; Al: Al_2O_3; Fe: Fayalite; Na: Albite; K: Orthoclase; Ti, Mn: $MnTiO_3$; Cr: Cr_2O_3; Ni: NiO), pyrite for Fe and S in sulfides, pure metals (Fe, Mn, Si, Mg, Ni, Cr) for metallic alloys, and andradite ($Ca_3Fe_2Si3O_{12}$) for oxygen. Analyses are given in Table S3.

3.3. Oxygen fugacity and sulfur fugacity determination

Sample intrinsic fO_2 values were determined after analysis using the compositions of co-existing metallic alloy and silicate melt, following the method described in Cartier et al. (2014b). In most of our samples, the FeO content of the silicate melt is lower than 1%, resulting in poor accuracy for FeO activity estimation. We therefore based our calculation on the following redox equilibrium:

$$Si^{metal\ alloy} + O_2 = SiO_2^{silicate\ melt} \quad (1)$$

The oxygen fugacity is calculated as

$$fO_2 = \exp\left(-\frac{\Delta G^\circ}{RT}\right) \cdot \left(\frac{a_{SiO_2}^{silicate\ melt}}{a_{Si}^{metal\ alloy}}\right) \quad (2)$$

ΔG° is the standard free-energy change of the reaction (1), T is the temperature of the experiment (K), and R is the gas constant. The activity of Si in solution in the metallic alloy $a_{Si}^{metal\ alloy}$ was determined using its concentration (Table S3) and the activity coefficient provided by the Metal Activity Calculator of the Oxford petrology group (Wade and Wood, 2005). The activity of silica $a_{SiO_2}^{silicate\ melt}$ is 1 because coesite is present in most experiments.

Oxygen fugacity values are expressed relatively to the iron-wüstite (IW) equilibrium (Huebner, 1971) such as:

$$\Delta IW = \log fO_2\,(experiment) - \log fO_2\,(IW) \quad (3)$$

The fO_2 values of the samples range from IW-1 to IW-8 (Table 1).

Sample intrinsic sulfur fugacities (fS_2) values were estimated relatively to the iron-troïlite (IT) buffer according to the following equation:

$$\Delta IT = \log fS_2\,(experiment) - \log fS_2\,(IT) = 2\log\left(\frac{a_{FeS}^{sulfide}}{a_{Fe}^{metal\ alloy}}\right) \quad (4)$$

$a_{Fe}^{metal\ alloy}$ and $a_{FeS}^{sulfide}$ correspond to the activity of Fe and FeS in the metal alloy and in the sulfide respectively. We calculated the $a_{Fe}^{metal\ alloy}$ with the Metal Activity Calculator (Wade and Wood, 2005) and made the assumption that the activity of FeS equals its mole fraction in the sulfide. The fS_2 values of the samples range from IT to IT + 1 (Table 1). These values mean that our samples are buffered at Fe-FeS by the presence of almost stoichiometric FeS sulfide. We therefore consider that the fS_2 parameter is fixed in our experimental series.

3.4. Experimental results

3.4.1. The composition of iron-rich alloys

In order to model Mercury core formation, we use metal-silicate partition coefficients in sulfide saturated systems. It is known that the presence of sulfur in Fe-alloys can strongly affect the partitioning of numerous trace elements, often enhancing their solubility in Fe alloys (Bouhifd et al., 2013; Laurenz et al., 2016; Mills et al., 2007), and this effect seems much more pronounced above ∼25 wt.% S in the alloy (this value roughly corresponds to the composition of the Fe-FeS eutectic, which is sensitive to pressure; Morard et al. 2007).

Most experimental samples contain 3 equilibrated melts: a silicate melt and two Fe-rich alloys, one containing Si and one of almost stoichiometric FeS composition (Fig. 3). This is because for fO_2 < IW Si dissolves in the Fe alloy (Kilburn and Wood, 1997) and at pressures ≤5 GPa Si and S are mutually exclusive in the metal phase (Kilburn and Wood, 1997; Morard and Katsura, 2010). Under moderately reducing conditions (>IW-2.5), very little Si partitions in the alloy, and S is siderophile. Sulfur solubility in the alloy is thus quite high and our experimental alloys contain up to 6 wt.% S (Fig. 4, Table S3). On the contrary under highly reducing conditions (<IW-2.5), important amounts of Si dissolve in the alloy, dramatically decreasing sulfur solubility in the metal phase at sulfide saturation (Fig. 4). Consequently, in these conditions relevant for Mercury's differentiation, there is a compositional gap between the FeS melt and the Fe(Si) melt that cannot contain more than ∼1.5 wt.% S (Fig. 4).

In the following we will compare our partitioning data with literature data also obtained in sulfide (FeS)-saturated systems. Some of our most reduced experiments however did not reach sulfide saturation because their bulk sulfur contents were diluted by the addition of important amounts of silicon, which decreased the oxygen fugacity and accordingly increased sulfur solubility in the equilibrium silicate melt (Namur et al., 2016a). Nevertheless we think these samples are very close to sulfide saturation as: a) their metallic alloys contain similar amounts of sulfur to similar samples (those from Namur et al., 2016a) which are sulfide saturated (Fig. 4) and b) the metal/silicate partition coefficients

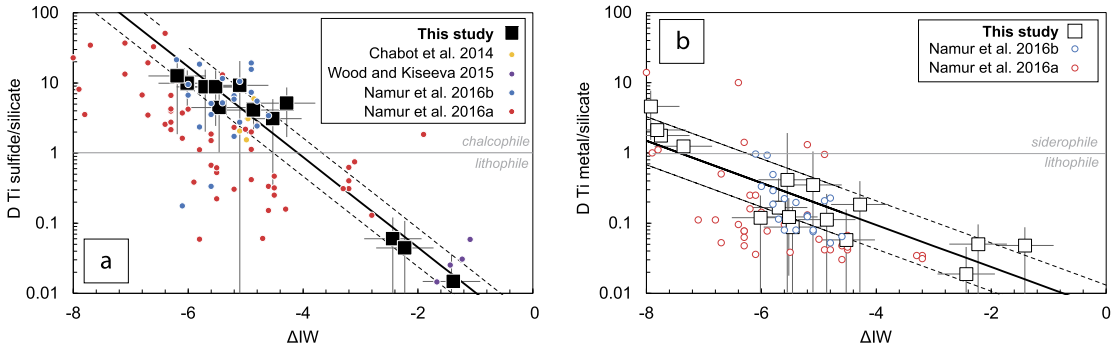

Fig. 5. Titanium metal/silicate (a) and sulfide/silicate (b) Nernst partition coefficients as a function of oxygen fugacity (ΔIW). Our experiments were performed at 5 GPa (except one experiment which was conducted at 3 GPa), at near liquidus temperatures, and are saturated with an FeS sulfide. Error bars correspond to ±1 sigma uncertainties on Ti data and fO_2 estimates. Literature data correspond to experiments conducted between 1 bar and 4 GPa, at various temperatures, and in FeS saturated systems. The thick lines represent the parameterizations of D(Ti) as a function of fO_2 based on 5 GPa experiments only and dotted lines their ±1 sigma uncertainties.

obtained in these samples are consistent with those obtained in sulfide-saturated experiments equilibrated at similar oxygen fugacity conditions (Fig. 5).

3.4.2. Titanium partitioning under reducing conditions

Titanium Nernst (i.e. calculated on weight % basis) metal/silicate and sulfide/silicate partition coefficients are presented in Table 1 and shown in Fig. 5 as a function of fO_2, together with literature data obtained in similar conditions (pressure between 1 bar and 5 GPa, FeS saturated systems). Under moderately reducing conditions (fO_2 > IW-3) Ti is lithophile with metal/silicate and sulfide/silicate partition coefficients being lower than 1. However, under extremely reducing conditions (at IW-8) Ti is siderophile and chalcophile. At Mercury's redox conditions (IW-5.4 ± 0.4; Namur et al., 2016a) Ti is chalcophile ($D^{sulfide/silicate} \approx 7$), but not siderophile even though its metal/silicate partitioning is not negligible ($D^{metal/silicate} \approx 0.1$). This particular behavior makes Ti an ideal tracer for the formation of a sulfide melt, i.e. if such a melt was extracted during Mercury's core formation, the silicate portion of the planet would be relatively depleted in Ti compared to chondrites. Moreover, as Ti is not siderophile in these conditions, any substantial depletion of Ti in the silicate portion could not be the consequence of metallic core formation.

It can be seen on Fig. 5 that there is important scatter of literature partitioning data around the general trends versus fO_2. We tested the effect of pressure, temperature, and S contents of the metal phases on these partition coefficients but found no correlation. We think this scatter is rather related to analytical issues, as these studies did not focus on Ti and Fe-S-rich alloys are particularly difficult to analyze because of their shapes and quench textures (Fig. 3). In order to quantify Ti partitioning, we therefore used only our new data obtained at 5 GPa (CMB pressure in Mercury).

The partitioning of Ti between silicate, metal and sulfide can be described by the following equilibria:

$$TiO_2 = Ti + O_2 \tag{5}$$

$$TiO_2 + S_2 = TiS_2 + O_2 \tag{6}$$

At fixed pressure and temperature, the equilibrium constants of these reactions are defined as:

$$K_{(5)} = \frac{a_{Ti}^{metal} \cdot fO_2}{a_{TiO_2}^{silicate}} \tag{7}$$

$$K_{(6)} = \frac{a_{TiS_2}^{sulfide}}{a_{TiO_2}^{silicate}} \cdot \frac{fO_2}{fS_2} \tag{8}$$

where a_{Ti}^{metal}, $a_{TiS_2}^{sulfide}$ and $a_{TiO_2}^{silicate}$ are the activities of Ti in the metal, TiS_2 in the sulfide and TiO_2 in the silicate respectively.

At equilibrium we have:

$$\frac{a_{Ti}^{metal}}{a_{TiO_2}^{silicate}} = e^{\frac{-\Delta G^{\circ}_{(5)}}{RT}} \cdot \frac{1}{fO_2} \tag{9}$$

$$\frac{a_{TiS_2}^{sulfide}}{a_{TiO_2}^{silicate}} = e^{\frac{-\Delta G^{\circ}_{(6)}}{RT}} \cdot \frac{fS_2}{fO_2} \tag{10}$$

where $-\Delta G^{\circ}_{(5)}$ and $-\Delta G^{\circ}_{(6)}$ are the standard free-energy changes of reactions 5 and 6, R is the ideal gas constant and T the temperature (K).

As Ti is a minor element in chondritic systems we made the assumption that it obeys Henry's law, i.e. its compound activities equal their mole fraction. This leads to:

$$\frac{a_{Ti}^{metal}}{a_{TiO_2}^{silicate}} \approx \frac{X_{Ti}^{metal}}{X_{TiO_2}^{silicate}} \propto D_{Ti}^{\frac{metal}{silicate}} \tag{11}$$

$$\frac{a_{TiS_2}^{sulfide}}{a_{TiO_2}^{silicate}} \approx \frac{X_{TiS_2}^{sulfide}}{X_{TiO_2}^{silicate}} \propto D_{Ti}^{\frac{sulfide}{silicate}} \tag{12}$$

where X_{Ti}^{metal}, $X_{TiS_2}^{sulfide}$ and $X_{TiO_2}^{silicate}$ are the molar fractions of Ti in the metal, TiS_2 in the sulfide and TiO_2 in the silicate respectively, $D_{Ti}^{\frac{metal}{silicate}}$ and $D_{Ti}^{\frac{sulfide}{silicate}}$ are the Nernst partition coefficients of Ti.

At fixed pressure, temperature and fS_2, we therefore have, by combining eq. (9) with eq. (11) and eq. (10) with eq. (12):

$$D_{Ti}^{\frac{metal}{silicate}} \propto \frac{1}{fO_2} \tag{13}$$

$$D_{Ti}^{\frac{sulfide}{silicate}} \propto \frac{1}{fO_2} \tag{14}$$

Thus we parameterized our Ti partition coefficients as a function of $1/fO_2$. This gives (Fig. 5):

$$\ln D_{Ti}^{metal/silicate} = [-0.6904 * \Delta IW - 5.124] \pm 0.7901 \tag{15}$$

$$\ln D_{Ti}^{sulfide/silicate} = [-1.483 * \Delta IW - 6.064] \pm 0.6297 \tag{16}$$

It is important to note that these parameterizations can only be used in the case of metal-silicate-sulfide (FeS) systems and at 5 GPa. Also, the errors associated to both parameterizations are significant, especially for $D_{Ti}^{metal/silicate}$, as can be seen in Fig. 5. These errors are taken into account in the models presented in the following part, and their effect on the model results are discussed in section 5.3.

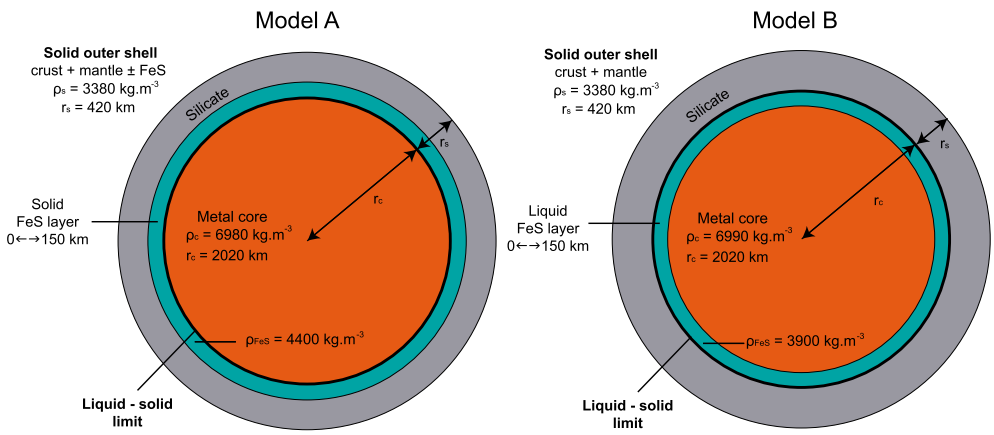

Fig. 6. Schematic representation of the two end-member models used to calculate elemental distribution during core formation. Mercury is made up of a metallic core, surrounded by a FeS layer and a silicate shell. (a) The solid outer shell consists of a silicate portion and a FeS solid layer with a thickness of 0 to 150 km. (b) The core consists of a metal sphere surrounded by a liquid FeS layer with a thickness of 0 to 150 km.

4. Modeling Mercury's core formation

In this section we present two models that we use to calculate element distribution during Mercury's core formation. Both models are 'single-step': we consider that the whole silicate magma ocean and core-forming melts are in equilibrium with each other. This assumption is realistic as Mercury has the size of a planetary embryo (Deguen et al., 2014; Rubie et al., 2011). The models make use of Ti and Al distribution (Al is used to normalize Ti abundances; see section 5) to discuss the potential existence of a FeS matte at the CMB and its likely thickness.

The main structure of the planet is constrained by geophysical data (Hauck et al., 2013): the metal core is about 2020 km in diameter and has a mean density of 6980 kg.m^{-3}. The outer solid shell is 420 km thick with a mean density of about 3380 kg.m^{-3} and consists of the crust, the mantle and a potential FeS layer with a thickness between 0 and 150 km with a density of 4400 kg.m^{-3} (Fig. 6(a)). In the second model we consider the possibility of a liquid FeS layer (with a density of 3900 kg.m^{-3}), which would be localized in the outer part of the core (Fig. 6(b)), therefore reducing the volume of the metallic core. In both cases, geophysical parameters constrain a mass for each of the 3 shells (silicate portion (mantle + crust), FeS layer and metallic core), in which the distribution of Ti and Al is calculated by using the experimental partition coefficients in the following equation:

$$m_X^{Silicate} = \frac{m_{Bulk\ X}}{m_{Mercury}} \cdot \frac{m_{Silicate}}{\frac{m_{Silicate}}{m_{Mercury}} + D_X^{\frac{sulfide}{silicate}} \cdot \frac{m_{FeS}}{m_{Mercury}} + D_X^{\frac{metal}{silicate}} \cdot \frac{m_{Metal}}{m_{Mercury}}} \quad (17)$$

where $m_X^{Silicate}$ = mass of element X contained in the silicate portion, $m_{Bulk\ X} = X$ bulk content in Mercury, $m_{Mercury}$ = Mercury's mass, $m_{Silicate}$ = mass of the silicate portion, m_{FeS} = mass of the FeS layer, m_{Metal} = mass of the metallic core, $D_X^{\frac{sulfide}{silicate}} = X$ sulfide/silicate partition coefficient, $D_X^{\frac{metal}{silicate}} = X$ metal/silicate partition coefficient. With equation (17), Ti and Al distributions are modeled individually, which means that we have to input values for the bulk Ti and Al contents of Mercury. However, the results are not sensitive to absolute bulk values as long as we keep a chondritic bulk Ti/Al ratio for the planet, as discussed in section 5.1.

To model the Ti distribution $D_{Ti}^{sulfide/silicate}$ and $D_{Ti}^{metal/silicate}$ are replaced in eq. (17) by the two parameterizations presented in section 3.4.2 (eq. (15) and eq. (16)). Al is considered as a pure lithophile element, entirely concentrated in the silicate portion of the planet. This assumption is justified by the fact that Al has never been detected in Fe-rich alloys, neither in our experiments nor in those from the literature. This is because extremely reducing conditions are needed to reduce Al^{3+} to Al^0 (at 1 bar and 1500 K the Al-Al_2O_3 equilibrium fO_2 is ∼IW-15).

5. Ti/Al as a tracer of sulfide layer formation

5.1. Ti/Al ratio of the bulk Mercury

As explained above, Ti can be used as a tracer for the formation of a sulfide layer because in the fO_2 conditions of Mercury's core formation, it is chalcophile but not siderophile. With our model, we can therefore calculate the depletion of this element in the bulk silicate shell of the planet, depending on the assumed thickness of the sulfide layer. MESSENGER measurements provided surface data but only relative element abundances. In order to link bulk silicate composition to surface element ratios, we therefore choose to normalize Ti to Al. Both elements are highly refractory, which means they are not fractionated by volatility-controlled processes during accretion (Lodders, 2003). This is illustrated by the constancy of the Ti/Al weight ratio among all classes of chondrites, which is equal to 0.058 ± 0.003 (mean value and standard deviation calculated with the data of Lodders and Fegley (1998) and Lauretta et al. (2009)). This range of 0.055 to 0.061 includes enstatite chondrites (Ti/Al = 0.056) and bencubbinites (Ti/Al = 0.060) which are the best candidates as Mercury's building blocks (Cartier and Wood, 2019; Malavergne et al., 2010; Taylor and Scott, 2003). This range also includes ordinary chondrites (Ti/Al = 0.058) and carbonaceous chondrites (Ti/Al = 0.057). It is therefore a reasonable hypothesis to consider that these elements are in chondritic proportions in bulk planets. This assumption was used to model the bulk composition of all the terrestrial planets (e.g. Morgan and Anders, 1980).

5.2. Ti/Al of the bulk silicate Mercury

Another reason to use Ti/Al ratio is that Ti and Al do not significantly fractionate from each other during the early stages of igneous differentiation, because their partition coefficients between the two main peridotite-forming minerals, olivine and pyroxene, and primary silicate melts are almost identical (Beattie, 1993; Bédard, 2005; Cartier et al., 2014b). As a consequence, primitive lavas such as terrestrial komatiites display relatively constant Ti/Al ratios (Arndt et al., 2008), and the Ti/Al ratio of the Earth's bulk crust (0.08 for the oceanic crust and 0.05 for the continental crust, Rudnick and Gao, 2003; White and Klein, 2013) is not very different

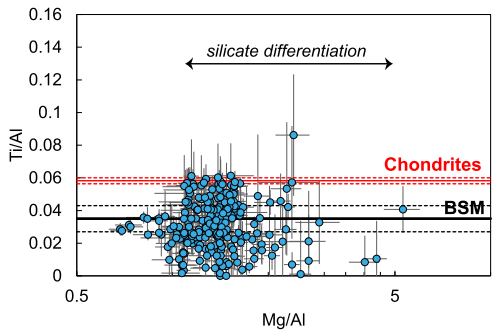

Fig. 7. Ti/Al of Mercury silicate portion. The blue points are MESSENGER measurements and the black lines correspond to our best estimate of the true surface Ti/Al ratio (BSM: Bulk Surface Mercury) and its uncertainty (0.0345 ± 0.008), estimated from our Monte Carlo simulations (e.g., Fig. 2). As Ti/Al is not fractionated by silicate differentiation, this value is therefore considered as representative of the bulk silicate composition of Mercury. The red lines correspond to the mean chondritic Ti/Al ratio and its standard deviation (calculated after the values given in Lodders and Fegley, 1998, Lauretta et al., 2007 and Lauretta et al., 2009).

from the chondritic ratio. As the secondary volcanic crust of Mercury formed by effusion of primitive lavas produced by high degree adiabatic decompression melting of a lherzolitic mantle (Charlier et al., 2013; Namur et al., 2016b), an analogy can be made with terrestrial primitive lavas and we therefore consider that the melt Ti/Al ratio is not significantly affected by the extent of the melting process. The constancy of Ti/Al ratios measured across Mercury's surface supports this hypothesis.

MESSENGER XRS measurements of Ti/Al are plotted against measured Mg/Al ratios from the same locations in Fig. 7. Mg/Al is here considered as a proxy of silicate igneous fractionation, with high Mg/Al lavas being produced by high degree partial melting and low Mg/Al lavas being produced by low degree partial melting (Palme and O'Neill, 2014). There is no indication of any correlation between Mg/Al and Ti/Al in Mercury lavas, confirming that Ti/Al in lavas can be used to estimate the bulk silicate ratio of the planet. We therefore use the mean value of these MESSENGER data to argue that the bulk silicate Mercury has a slightly subchondritic Ti/Al ratio of 0.035 ± 0.008 (Fig. 2).

5.3. Model results and likely absence of a FeS layer in Mercury

In Fig. 8, we compare the average bulk silicate Ti/Al ratio obtained from MESSENGER data to the calculated Ti/Al ratio of the silicate portion as a function of the FeS layer thickness as predicted by the two models (see details in Fig. 6). In order to interpret the results, the errors associated with the models and surface data must be considered. In both models, there are three sources of uncertainty: a) the assumed chondritic bulk Ti/Al ratio (0.058 ± 0.003) of Mercury, b) the intrinsic fO_2 of Mercury (IW-5.4 $\pm$ 0.4) and c) the Ti partition coefficients (sulfide/silicate and metal/silicate, see section 3.4.2). Oxygen fugacity and partition coefficients have the greatest impact on the numerical results while the error on the bulk Ti/Al is negligible. Oxygen fugacity and partition coefficients are also linked by the parameterizations described in section 3.4.2, which prevents the use of a classical calculation of propagation of uncertainty. To estimate the statistical error associated with the results we therefore conducted 10000 Monte Carlo simulations for each model, generating random numbers from the normal distribution of each parameter (bulk Ti/Al, fO_2, $D_{Ti}^{sulfide/silicate}$, $D_{Ti}^{metal/silicate}$). We then calculated the bounds containing 68% of the solutions (corresponding to the ± 1 standard deviation area in the case of a normal distribution), those containing 95% of the solutions (± 2 standard deviations), and those containing 99.5% of the solutions (± 3 standard deviations). The 68% confidence bounds of both models are presented on Fig. 8, together with the bulk silicate Mercury Ti/Al and its associated standard deviation. The cumulative probability function of the expected value of the FeS layer is then evaluated as the overlapping of MESSENGER data and geochemical model statistical distribution repartitions.

Fig. 9 shows the cumulative distribution function of the FeS layer thickness for both models. These figures mean that, taking into account the error associated to both models and MESSENGER data, the most likely scenario is that Mercury does not have a FeS layer (52^{+25}_{-23}% probability that the FeS layer is 0 km thick with model A, and 53^{+26}_{-19}% probability with model B). If however there was a sulfide layer, it would probably not be thicker than a few kilometers, as there are 68^{+23}_{-28}% probability that the sulfide layer thickness is <11 km with model A and 68^{+22}_{-24}% probability that the sulfide layer thickness is <13 km with model B. Finally our models show it is statistically impossible that a thick sulfide layer formed as there are $99.5^{+0.4}_{-4}$% probability that the sulfide layer thickness is <101 km with model A and $99.5^{+0.4}_{-1}$% probability that the sulfide layer thickness is <134 km with model A.

Considering that no FeS extraction occurred during core formation (i.e. FeS layer thickness = 0 km), the model reproduces the slightly subchondritic Ti/Al of the bulk silicate Mercury. This subchondritic ratio can thus be explained by the selective extraction of Ti by the metallic core: although Ti is not siderophile at reducing conditions, its metal/silicate partitioning is not negligible and because of the very large proportion of Mercury's core, the starting chondritic Ti/Al is slightly affected.

Malavergne et al. (2014) proposed that not only a FeS phase would form during Mercury's early differentiation, but a Mg-Fe-Ca-rich sulfide could also be part of the magma ocean equilibrium, together with the metal and the silicate melts, this idea being supported by the detection of such a phase in highly reducing experiments (Berthet et al., 2009; Malavergne et al., 2014; McCoy et al., 1999; Namur et al., 2016a). This phase would virtually retain a few weight percent of Fe in the mantle, bringing a solution to Mercury's "iron paradox" (i.e. Mercury is highly reduced so its silicate should contain much less than the average 1.5 wt.% Fe observed by MESSENGER at the surface). This hypothesis requires that Mercury's building blocks contained more than 4 wt.% S (Namur et al., 2016a) to ensure (Mg,Fe,Ca)S saturation in the deep magma ocean. Also, in order to match the observed S and Fe contents at the surface (Nittler et al., 2018), about 2 wt.% of the (Mg,Fe,Ca)S should be extracted from the mantle and carried by magmas ascending toward the surface (Malavergne et al., 2014). In this scenario, the Ti/Al of the silicate portion of Mercury would first be highly fractionated ($Ti/Al < 0.01$) by the selective extraction of Ti by the FeS and the (Mg,Fe,Ca)S phase, as it has been shown that Ti is compatible in both phases under highly reducing conditions (McCoy et al., 1999; Vander Kaaden and McCubbin, 2016). Then, the silicate magma ocean would crystallize to form a sulfide-bearing lherzolitic mantle (Namur et al., 2016b), which would eventually undergo partial melting to produce the secondary lavas making most of Mercury's crust. The lavas would have the same very low Ti/Al as the mantle because the high degree of partial melting is unable to fractionate Ti from Al, and the ~2 wt.% (Mg,Fe,Ca)S carried by these lavas would enhance the Ti/Al of the mix. However, given the Ti solubility in these sulfides (~0.5 wt.%, McCoy et al., 1999) and the weak contribution of these sulfides to the surface lithologies (~2 wt.%), the Ti/Al observed by MESSENGER would be only slightly greater than the Ti/Al of the silicate portion only. Thus if this scenario happened, one would still expect a very low Ti/Al at the surface, which is not observed. Therefore our model does not support the idea of the formation of (Mg,Fe,Ca)S phases in addition to FeS during core formation.

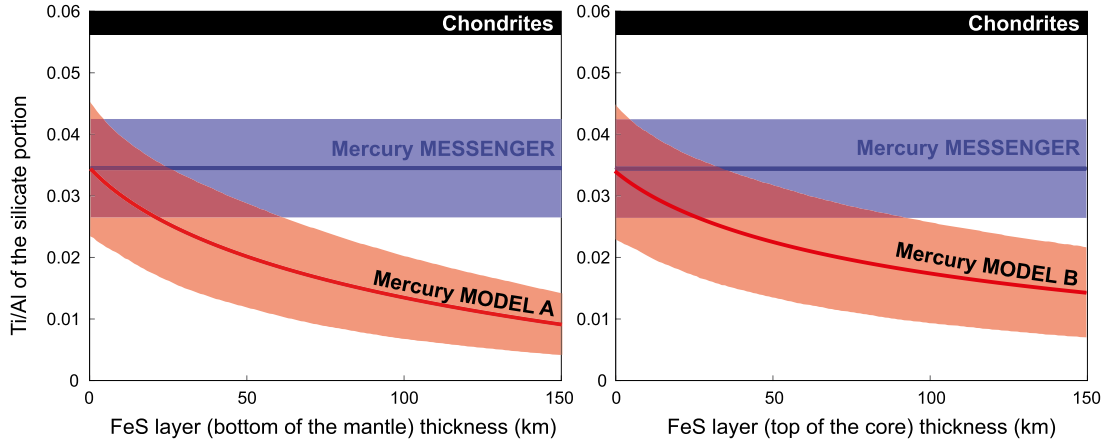

Fig. 8. Results of the two models used to calculate Ti and Al relative contents in the silicate portion of Mercury as a function of the FeS layer thickness. Red thick solid curves correspond to the median of Monte Carlo simulations. Uncertainty associated to the model results is represented by the red area limited by the 68% confidence bounds. The blue line is the bulk silicate Mercury Ti/Al and the light blue strip the $\pm 1\sigma$. In both scenarios the best match between Mercury data and our models corresponds to no (0 km) FeS layer. The slightly subchondritic Ti/Al of Mercury's silicate is explained by the selective extraction of Ti by the metallic core under reducing conditions.

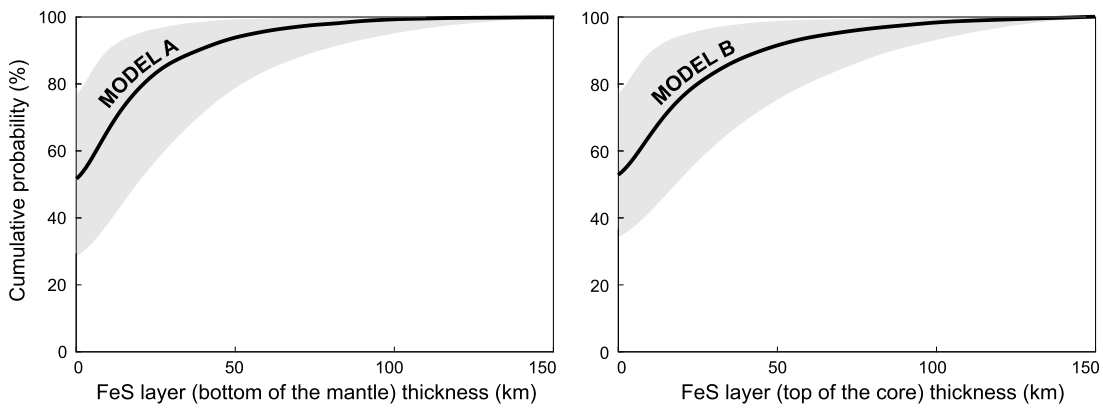

Fig. 9. Cumulative distribution of the expected FeS layer thickness for model A and model B and associated ± 1 standard deviation (gray strips). The most likely scenario is that Mercury does not have a FeS layer (52^{+25}_{-23}% chances the FeS layer is 0 km thick with model A, and 53^{+26}_{-19}% chances with model B). If however there was a sulfide layer, it would probably not be thicker than few kilometers, as there are 68^{+23}_{-28}% chances that the sulfide layer thickness is <11 km with model A and 68^{+22}_{-24}% chances that the sulfide layer thickness is <13 km with model B.

A last scenario that we considered consists of the late precipitation of (Mg, Fe, Ca)S sulfides during fractional crystallization of an initially sulfur-undersaturated magma ocean (Boukaré et al., 2019). This case corresponds to a bulk magma ocean containing $\leq$8% S (and a bulk Mercury containing $\leq$3% S, Namur et al., 2016a). In this case no FeS melt would have exsolved during core formation, and the precipitation of sulfides would occur only when the sulfur content of the residual silicate melt of the magma ocean would have reached sulfur solubility. In this context, Boukaré et al. (2019) modeled the crystallization of a magma ocean initially containing 5 wt.% S and with a fixed fO_2 of IW-6 which would start to precipitate sulfides at around half of the CMB depth. Applying the same mass balance calculation as for the previous scenario, surface lavas would display a Ti/Al ratio of 0.02. For a magma ocean initially containing 1 wt.% S, sulfides would start precipitating at very shallow depth (1/4 of the CMB depth, Boukaré et al., 2019) and surface lavas would display a Ti/Al ratio of 0.04. We therefore suggest that the precipitation of (Mg, Fe, Ca)S during cooling of the magma ocean does not fractionate the Ti/Al ratio of the magma very strongly and certainly not as much as to core formation. The lack of geophysical, petrological and geochemical constrains hamper exploring further the hypothesis of a S-undersaturated Mercurian magma ocean, although it is the scenario supported by our model and MESSENGER data.

It should be noted that these models do not give information about the potential formation of a secondary liquid sulfide layer after core formation by exsolution of FeS from the FeSi metallic alloy during core cooling and crystallization (Dumberry and Rivoldini, 2015; Knibbe and Westrenen, 2018). Under conditions of Mercury's core formation, the sulfur solubility in the metallic alloy at sulfide saturation is very low ($\sim$1.5 wt.%, Fig. 4) which gives an upper limit for sulfur content of Mercury's bulk core. While the solid inner core crystallizes, sulfur is progressively enriched in the remaining liquid (Morard et al., 2008) and can quickly reach sulfide saturation. Estimating the thickness of a secondary FeS layer is made impossible by the absence of detailed knowledge of the core composition and degree of crystallization. Nevertheless, the formation of such an exsolved layer would have fewer implications than a primary FeS layer as it would have no impact on the composition of the silicate fraction and on the distribution of heat producing elements in Mercury.

6. Conclusions and perspectives

We have presented a new data set consisting of 233 Ti/Si measurements from across Mercury's surface made by the X-ray Spectrometer on the MESSENGER spacecraft. Coupling these data with XRS Mg/Si and Al/Si data we showed that the Ti/Al measured at Mercury's surface is representative of the bulk silicate Mercury,

which displays a slightly subchondritic Ti/Al ratio of 0.035 ± 0.008 (compared to a chondritic ratio of ∼0.058). We conducted multiphase equilibria experiments to show that in the conditions of Mercury's core formation, Ti is chalcophile but not siderophile, making Ti a useful tracer of a sulfide melt formation. We parameterized and used our partitioning data in a model to calculate the relative depletion of Ti in the bulk silicate Mercury as a function of a putative FeS layer thickness. By comparing the model results and surface data we showed that the most likely scenario is that Mercury does not have a FeS layer, or one that would only be a few kilometers thick (<13 km). We also showed that Mercury's metallic core cannot contain more than ∼1.5 wt.% sulfur and that the formation of this core under reducing conditions is likely responsible for the slight lowering of the Ti/Al ratio from the chondritic value, as measured in the silicate portion of the planet.

Based on our new view of the chemical and physical structure of Mercury's core, it would be important to model the distribution of the heat producing elements (K, U, Th) during Mercury's early differentiation. Unfortunately K, Th and U partitioning data between silicate, Fe(Si) and FeS alloys are lacking for conditions relevant for Mercury core-mantle equilibrium (5 GPa – very reducing conditions). Experiments should therefore be conducted in the right conditions and partitioning data integrated in a model. Only then could the K, U and Th abundances measured at the surface of Mercury be fully interpreted.

Declaration of competing interest

The authors declare that they have no known competing financial interests or personal relationships that could have appeared to influence the work reported in this paper.

Acknowledgements

T. Hammouda and M. Boyet are acknowledged for their help with experiments, analysis and discussion. This research received funding from the European Research Council under the European Community's Seventh Framework Programme (FP7/2007-2013 Grant Agreement 209035) and from the French PNP program (INSU-CNRS). The multianvil apparatus of Laboratoire Magmas et Volcans is financially supported by the Centre National de la Recherche Scientifique (Instrument National de l'INSU). This research has been supported by the BRAIN-be program of the Belgian Science Policy Office (BR/143/A2/COME-IN). B.C. is a Research Associate of the Belgian Fund for Scientific Research-FNRS. O.N. acknowledges support from the FWO.

Appendix A. Supplementary material

Supplementary material related to this article can be found online at https://doi.org/10.1016/j.epsl.2020.116108.

References

Albarède, F., 2009. Volatile accretion history of the terrestrial planets and dynamic implications. Nature 461, 1227–1233. https://doi.org/10.1038/nature08477.

Anderson, J.D., Colombo, G., Esposito, P.B., Lau, E.L., Trager, G.B., 1987. The mass, gravity field, and ephemeris of Mercury. Icarus 71, 337–349.

Anderson, B.J., Johnson, C.L., Korth, H., Winslow, R.M., Borovsky, J.E., Purucker, M.E., Slavin, J.A., Solomon, S.C., Zuber, M.T., McNutt, R.L., 2012. Low-degree structure in Mercury's planetary magnetic field. J. Geophys. Res., Planets 117, 1–17. https://doi.org/10.1029/2012JE004159.

Andrault, D., Bolfan-Casanova, N., Nigro, G. Lo, Bouhifd, M.A., Garbarino, G., Mezouar, M., 2011. Solidus and liquidus profiles of chondritic mantle: implication for melting of the Earth across its history. Earth Planet. Sci. Lett. 304, 251–259. https://doi.org/10.1016/j.epsl.2011.02.006.

Arndt, N., Lesher, C.M., Barnes, S.J., 2008. Komatiite. Cambridge University Press.

Beattie, P., 1993. Olivine-melt and orthopyroxene-melt equilibria. Contrib. Mineral. Petrol. 115, 103–111. https://doi.org/10.1007/BF00712982.

Bédard, J.H., 2005. Partitioning coefficients between olivine and silicate melts. Lithos 83, 394–419. https://doi.org/10.1016/j.lithos.2005.03.011.

Berthet, S., Malavergne, V., Righter, K., 2009. Melting of the Indarch meteorite (EH4 chondrite) at 1 GPa and variable oxygen fugacity: implications for early planetary differentiation processes. Geochim. Cosmochim. Acta 73, 6402–6420. https://doi.org/10.1016/j.gca.2009.07.030.

Bouhifd, M.A., Andrault, D., Bolfan-Casanova, N., Hammouda, T., Devidal, J.L., 2013. Metal-silicate partitioning of Pb and U: effects of metal composition and oxygen fugacity. Geochim. Cosmochim. Acta 114, 13–28. https://doi.org/10.1016/j.gca.2013.03.034.

Boujibar, A., Andrault, D., Bouhifd, M.A., Bolfan-Casanova, N., Devidal, J.-L., Trcera, N., 2014. Metal-silicate partitioning of sulphur, new experimental and thermodynamic constraints on planetary accretion. Earth Planet. Sci. Lett. 391, 42–54. https://doi.org/10.1016/j.epsl.2014.01.021.

Boujibar, A., Habermann, M., Righter, K., Kent Ross, D., Pando, K., Righter, M., Chidester, B.A., Danielson, L.R., 2019. U, Th, and K partitioning between metal, silicate, and sulfide and implications for Mercury's structure, volatile content, and radioactive heat production. Am. Mineral. 104, 1221–1237.

Boukaré, C.-E., Parman, S.W., Parmentier, E.M., Anzures, B.A., 2019. Production and preservation of sulfide layering in Mercury's mantle. J. Geophys. Res., Planets.

Brown, S.M., Elkins-Tanton, L.T., 2009. Compositions of Mercury's earliest crust from magma ocean models. Earth Planet. Sci. Lett. 286, 446–455. https://doi.org/10.1016/j.epsl.2009.07.010.

Byrne, P.K., Ostrach, L.R., Fassett, C.I., Chapman, C.R., Denevi, B.W., Evans, A.J., Klimczak, C., Banks, M.E., Head, J.W., Solomon, S.C., 2016. Widespread effusive volcanism on Mercury likely ended by about 3.5 Ga. Geophys. Res. Lett. 43, 7408–7416. https://doi.org/10.1002/2016GL069412.

Cartier, C., Hammouda, T., Boyet, M., Bouhifd, M.A., Devidal, J.L., 2014a. Redox control of the fractionation of niobium and tantalum during planetary accretion and core formation. Nat. Geosci. 7, 573–576. https://doi.org/10.1038/ngeo2195.

Cartier, C., Hammouda, T., Doucelance, R., Boyet, M., Devidal, J.L., Moine, B., 2014b. Experimental study of trace element partitioning between enstatite and melt in enstatite chondrites at low oxygen fugacities and 5 GPa. Geochim. Cosmochim. Acta 130, 167–187. https://doi.org/10.1074/jbc.RA117.000808.

Cartier, C., Wood, B.J., 2019. The role of reducing conditions in building Mercury. Elements.

Chabot, N.L., Wollack, E.A., Klima, R.L., Minitti, M.E., 2014. Experimental constraints on Mercury's core composition. Earth Planet. Sci. Lett. 390, 199–208. https://doi.org/10.1016/j.epsl.2014.01.004.

Charlier, B., Grove, T.L., Zuber, M.T., 2013. Phase equilibria of ultramafic compositions on Mercury and the origin of the compositional dichotomy. Earth Planet. Sci. Lett. 363, 50–60. https://doi.org/10.1016/j.epsl.2012.12.021.

Charlier, B., Namur, O., 2019. The origin and differentiation of planet Mercury. Elements 15, 9–14. https://doi.org/10.2138/gselements.15.1.9.

Deguen, R., Landeau, M., Olson, P., 2014. Turbulent metal–silicate mixing, fragmentation, and equilibration in magma oceans. Earth Planet. Sci. Lett. 391, 274–287. https://doi.org/10.1016/j.epsl.2014.02.007.

Dumberry, M., Rivoldini, A., 2015. Mercury's inner core size and core-crystallization regime. Icarus 248, 254–268. https://doi.org/10.1016/j.icarus.2014.10.038.

Evans, L.G., Peplowski, P.N., Rhodes, E.A., Lawrence, D.J., McCoy, T.J., Nittler, L.R., Solomon, S.C., Sprague, A.L., Stockstill-Cahill, K.R., Starr, R.D., Weider, S.Z., Boynton, W.V., Hamara, D.K., Goldsten, J.O., 2012. Major-element abundances on the surface of Mercury: results from the messenger gamma-ray spectrometer. J. Geophys. Res., Planets 117, 1–14. https://doi.org/10.1029/2012JE004178.

Frank, E.A., Potter, R.W.K., Abramov, O., James, P.B., Klima, R.L., Mojzsis, S.J., Nittler, L.R., 2017. Evaluating an impact origin for Mercury's high-magnesium region. J. Geophys. Res., Planets 122, 614–632. https://doi.org/10.1002/2016JE005244.

Genova, A., Goossens, S., Mazarico, E., Neumann, G.A., Kuang, W., Sabaka, T.J., Smith, D.E., Solomon, S.C., Zuber, M.T., Lemoine, F.G., 2019. Geodetic evidence that Mercury has a solid inner core. https://doi.org/10.1029/2018GL081135.

Hammouda, T., Chantel, J., Devidal, J.L., 2010. Apatite solubility in carbonatitic liquids and trace element partitioning between apatite and carbonatite at high pressure. Geochim. Cosmochim. Acta 74, 7220–7235. https://doi.org/10.1016/j.gca.2010.09.032.

Hauck, S.A., Margot, J.L., Solomon, S.C., Phillips, R.J., Johnson, C.L., Lemoine, F.G., Mazarico, E., McCoy, T.J., Padovan, S., Peale, S.J., Perry, M.E., Smith, D.E., Zuber, M.T., 2013. The curious case of Mercury's internal structure. J. Geophys. Res., Planets 118, 1204–1220. https://doi.org/10.1002/jgre.20091.

Huebner, J.S., 1971. Buffering techniques for hydrostatic systems at elevated pressures. In: Ulmer, G.C. (Ed.), Research Techniques for High Pressure and High Temperature, pp. 123–177.

Kilburn, M.R., Wood, B.J., 1997. Metal – silicate partitioning and the incompatibility of S and Si during core formation. Earth Planet. Sci. Lett. 152, 139–148.

Knibbe, J.S., van Westrenen, W., 2018. The thermal evolution of Mercury's Fe–Si core. Earth Planet. Sci. Lett. 482, 147–159. https://doi.org/10.1016/j.epsl.2017.11.006.

Knibbe, J.S., Westrenen, W., 2016. The interior configuration of planet Mercury constrained by moment of inertia and planetary. https://doi.org/10.1002/2015JE004908.

Laurenz, V., Rubie, D.C., Frost, D.J., Vogel, A.K., 2016. The importance of sulfur for the behavior of highly-siderophile elements during Earth's differentiation. Geochim. Cosmochim. Acta 194, 123–138. https://doi.org/10.1016/j.gca.2016.08.012.

Lauretta, D.S., Goreva, J.S., Hill, D.H., Killgore, M., 2007. Bulk compositions of the CB chondrites Bencubbin, Fountain Hills, MAC 02675, and MIL 05082. In: Lunar and Planetary Science Conference.

Lauretta, D.S., Goreva, J.S., Hill, D.H., Killgore, M., Blue, A.R.L.A., Campbell, A., Greenwood, R.C., Verchovsky, A.B., Franchi, I.A., 2009. The Fountain Hills unique CB chondrite: insights into thermal processes on the CB parent body. Meteorit. Planet. Sci. 44, 823–838.

Lodders, K., 2003. Solar system abundances and condensation temperatures of the elements. Astrophys. J. 591 (2), 1220–1247.

Lodders, K., Fegley, B., 1998. The Planetary Scientist's Companion, Oxford Uni. ed.

Malavergne, V., Cordier, P., Righter, K., Brunet, F., Zanda, B., Addad, A., Smith, T., Bureau, H., Surblé, S., Raepsaet, C., Charon, E., Hewins, R.H., 2014. How Mercury can be the most reduced terrestrial planet and still store iron in its mantle. Earth Planet. Sci. Lett. 394, 186–197. https://doi.org/10.1016/j.epsl.2014.03.028.

Malavergne, V., Toplis, M.J., Berthet, S., Jones, J., 2010. Highly reducing conditions during core formation on Mercury: implications for internal structure and the origin of a magnetic field. Icarus 206, 199–209. https://doi.org/10.1016/j.icarus.2009.09.001.

Manthilake, G., Chantel, J., Monteux, J., Andrault, D., Bouhifd, M.A., 2019. Thermal conductivity of FeS and its implications for Mercury's long - sustaining magnetic field. J. Geophys. Res., Planets, 1–10. https://doi.org/10.1029/2019JE005979.

Marchi, S., Chapman, C.R., Fassett, C.I., Head, J.W., Bottke, W.F., Strom, R.G., 2015. Global resurfacing of Mercury 4.0–4.1 billion years ago by heavy bombardment and volcanism. Nature, 24–26. https://doi.org/10.1038/nature12280.

Margot, J., Hauck, S.A., Mazarico, E., Padovan, S., Peale, S.J., 2018. Mercury's internal structure. In: Solomon, S.C., Anderson, B.J., Nittler, L.R. (Eds.), The View After MESSENGER.

McCoy, J., Dickinson, L., Lofgren, E., 1999. Partial melting of the Indarch (EH4) meteorite: a textural, chemical, and phase relations view of melting and melt migration. Meteorit. Planet. Sci. 34 (5), 735–746.

McCubbin, F.M., Riner, M.A., Kaaden, K.E. Vander, Burkemper, L.K., 2012. Is Mercury a volatile-rich planet? 39, 1–5. https://doi.org/10.1029/2012GL051711.

Mills, N.M., Agee, C.B., Draper, D.S., 2007. Metal-silicate partitioning of cesium: implications for core formation. Geochim. Cosmochim. Acta 71, 4066–4081. https://doi.org/10.1016/j.gca.2007.05.024.

Morard, G., Andrault, D., Guignot, N., Sanloup, C., Mezouar, M., Petitgirard, S., Fiquet, G., 2008. In situ determination of Fe-Fe3S phase diagram and liquid structural properties up to 65 GPa. Earth Planet. Sci. Lett. 272, 620–626. https://doi.org/10.1016/j.epsl.2008.05.028.

Morard, G., Katsura, T., 2010. Pressure–temperature cartography of Fe–S–Si immiscible system. Geochim. Cosmochim. Acta 74, 3659–3667. https://doi.org/10.1016/j.gca.2010.03.025.

Morard, G., Sanloup, C., Fiquet, G., Mezouar, M., 2007. Structure of eutectic Fe–FeS melts to pressures up to 17 GPa: Implications for planetary cores. Earth Planet. Sci. Lett. 263, 128–139. https://doi.org/10.1016/j.epsl.2007.09.009.

Morgan, J.W., Anders, E., 1980. Chemical composition of Earth, Venus, and Mercury. Proc. Natl. Acad. Sci. USA 77, 6973–6977. https://doi.org/10.1073/pnas.77.12.6973.

Namur, O., Charlier, B., 2017. Silicate mineralogy at the surface of Mercury. Nat. Geosci. 10. https://doi.org/10.1038/NGEO2860.

Namur, O., Charlier, B., Holtz, F., Cartier, C., Mccammon, C., 2016a. Sulfur solubility in reduced mafic silicate melts: implications for the speciation and distribution of sulfur on Mercury. Earth Planet. Sci. Lett. 448, 102–114. https://doi.org/10.1016/j.epsl.2016.05.024.

Namur, O., Collinet, M., Charlier, B., Grove, T.L., Holtz, F., Mccammon, C., 2016b. Melting processes and mantle sources of lavas on Mercury. Earth Planet. Sci. Lett. 439, 117–128. https://doi.org/10.1016/j.epsl.2016.01.030.

Nittler, L.R., Chabot, N.L., Grove, T.L., Peplowski, P.N., 2018. The chemical composition of Mercury. In: Solomon, S.C., Nittler, L.R., Anderson, B.J. (Eds.), Mercury - The View After MESSENGER, pp. 30–51.

Nittler, L.R., Frank, E.A., Weider, S.Z., Crapster-pregont, E.J., Vorburger, A., Starr, R.D., Solomon, S.C., 2016. Global major - element maps of Mercury updated from four years of MESSENGER X-ray observations. In: Lunar and Planetary Science Conference, pp. 2–3. https://doi.org/10.1016/j.icarus.2007.12.027.

Nittler, L.R., Starr, R.D., Weider, S.Z., McCoy, T.J., Boynton, W.V., Ebel, D.S., Ernst, C.M., Evans, L.G., Goldsten, J.O., Hamara, D.K., Lawrence, D.J., McNutt, R.L., Schlemm, C.E., Solomon, S.C., Sprague, A.L., 2011. The major-element composition of Mercury's surface from MESSENGER X-ray spectrometry. Science 333, 1847–1850. https://doi.org/10.1126/science.1211567.

O'Neill, H.S., 1991. The origin of the moon and the early history of the Earth—a chemical model. Part 2: the Earth. Geochim. Cosmochim. Acta 55, 1159–1172. https://doi.org/10.1016/0016-7037(91)90169-6.

Palme, H., O'Neill, H.S.C., 2014. Cosmochemical estimates of mantle composition. In: Treatise on Geochemistry, second edition, pp. 1–39.

Peplowski, P.N., Evans, L.G., Hauck, S.A., McCoy, T.J., Boynton, W.V., Gillis-Davis, J.J., Ebel, D.S., Goldsten, J.O., Hamara, D.K., Lawrence, D.J., McNutt, R.L., Nittler, L.R., Solomon, S.C., Rhodes, E.A., Sprague, A.L., Starr, R.D., Stockstill-Cahill, K.R., 2011. Radioactive elements on Mercury's surface from MESSENGER: implications for the planet's formation and evolution. Science 80 (333), 1850–1852. https://doi.org/10.1126/science.1211576.

Peplowski, P.N., Klima, R.L., Lawrence, D.J., Ernst, C.M., Denevi, B.W., Frank, E.A., Goldsten, J.O., Murchie, S.L., Nittler, L.R., Solomon, S.C., 2016. Remote sensing evidence for an ancient carbon-bearing crust on Mercury. Nat. Geosci. 9. https://doi.org/10.1038/NGEO2669.

Peplowski, P.N., Rhodes, E.A., Hamara, D.K., Lawrence, D.J., Evans, L.G., Nittler, L.R., Solomon, S.C., 2012. Aluminum abundance on the surface of Mercury: application of a new background-reduction technique for the analysis of gamma-ray spectroscopy data. J. Geophys. Res., Planets 117, 1–13. https://doi.org/10.1029/2012JE004181.

Pommier, A., Leinenweber, K., Tran, T., 2019. Mercury's thermal evolution controlled by an insulating liquid outermost core? 517, 125–134.

Rivoldini, A., Van Hoolst, T., 2013. The interior structure of Mercury constrained by the low-degree gravity field and the rotation of Mercury. Earth Planet. Sci. Lett. 377–378, 62–72. https://doi.org/10.1016/j.epsl.2013.07.021.

Rubie, D.C., Frost, D.J., Mann, U., Asahara, Y., Nimmo, F., Tsuno, K., Kegler, P., Holzheid, A., Palme, H., 2011. Heterogeneous accretion, composition and core–mantle differentiation of the Earth. Earth Planet. Sci. Lett. 301, 31–42. https://doi.org/10.1016/j.epsl.2010.11.030.

Rubie, D.C., Laurenz, V., Jacobson, S.A., Morbidelli, A., Palme, H., Vogel, A.K., Frost, D.J., 2016. Highly siderophile elements were stripped from Earth's mantle by iron sulfide segregation. Science 80 (353), 1141–1144. https://doi.org/10.1126/science.aaf6919.

Rudnick, R.L., Gao, S., 2003. Composition of the continental crust. In: Treatise on Geochemistry, vol. 3, pp. 1–64.

Savage, P.S., Moynier, F., Chen, H., Shofner, G., Siebert, J., Badro, J., Puchtel, I.S., 2015. Copper isotope evidence for large-scale sulphide fractionation during Earth's differentiation. Geochem. Perspect. Lett., 53–64. https://doi.org/10.7185/geochemlet.1506.

Smith, D.E., Zuber, M.T., Phillips, R.J., Solomon, S.C., Hauck, S.A., Lemoine, F.G., Mazarico, E., Neumann, G.A., Peale, S.J., Margot, J.-L., Johnson, C.L., Torrence, M.H., Perry, M.E., Rowlands, D.D., Goossens, S., Head, J.W., Taylor, A.H., 2012. Gravity field and internal structure of Mercury from MESSENGER. Science 80 (336), 214–217. https://doi.org/10.1126/science.1218809.

Taylor, G.J., Boynton, W.V., Brückner, J., Wänke, H., Dreibus, G., Kerry, K.E., Keller, J.M., Reedy, R.C., Evans, L.G., Starr, R.D., Squyres, S.W., Karunatillake, S., Gasnault, O., Maurice, S., D'Uston, C., Englert, P., Dohm, J.M., Baker, V., Hamara, D., Janes, D.M., Sprague, A.L., Kim, K.J., Drake, D., 2006. Bulk composition and early differentiation of Mars. J. Geophys. Res., Planets 111, 1–16. https://doi.org/10.1029/2005JE002645.

Taylor, G.J., Scott, E.R.D., 2003. Mercury. In: Treatise on Geochemistry. Pergamon, pp. 477–485.

Tosi, N., Grott, M., Plesa, A., Breuer, D., 2013. Thermochemical evolution of Mercury's interior. J. Geophys. Res., Planets 118, 2474–2487. https://doi.org/10.1002/jgre.20168.

Vander Kaaden, K.E., McCubbin, F.M., 2016. The origin of boninites on Mercury: an experimental study of the northern volcanic plains lavas. Geochim. Cosmochim. Acta 173, 246–263. https://doi.org/10.1016/j.gca.2015.10.016.

Wade, J., Wood, B.J., 2005. Core formation and the oxidation state of the Earth. Earth Planet. Sci. Lett. 236, 78–95. https://doi.org/10.1016/j.epsl.2005.05.017.

Weider, S.Z., Nittler, L.R., Starr, R.D., Crapster-pregont, E.J., Peplowski, P.N., Denevi, B.W., Head, J.W., Byrne, P.K., Hauck, S.A., Ebel, D.S., Solomon, S.C., 2015. Evidence for geochemical terranes on Mercury: global mapping of major elements with MESSENGER' s X-ray spectrometer. Earth Planet. Sci. Lett. 416, 109–120. https://doi.org/10.1016/j.epsl.2015.01.023.

Weider, S.Z., Nittler, L.R., Starr, R.D., McCoy, T.J., Solomon, S.C., 2014. Variations in the abundance of iron on Mercury's surface from MESSENGER X-ray spectrometer observations. Icarus 235, 170–186. https://doi.org/10.1016/j.icarus.2014.03.002.

Weider, S.Z., Nittler, L.R., Starr, R.D., McCoy, T.J., Stockstill-cahill, K.R., Byrne, P.K., Denevi, B.W., Head, J.W., Solomon, S.C., 2012. Chemical heterogeneity on Mercury's surface revealed by the MESSENGER X-ray spectrometer. J. Geophys. Res., Planets 117, 1–15. https://doi.org/10.1029/2012JE004153.

White, W.M., Klein, E.M., 2013. Composition of the oceanic crust. In: Treatise on Geochemistry, second edition. Elsevier Ltd.

Wohlers, A., Wood, B.J., 2017. Uranium, thorium and REE partitioning into sulfide liquids: implications for reduced S-rich bodies. Geochim. Cosmochim. Acta. https://doi.org/10.1016/j.gca.2017.01.050.

Wohlers, A., Wood, B.J., 2015. A Mercury-like component of early Earth yields uranium in the core and high mantle 142 Nd. https://doi.org/10.1038/nature14350.

Zolotov, M.Y., Sprague, A.L., Ii, S.A.H., Nittler, L.R., Solomon, S.C., Weider, S.Z., 2013. The redox state, FeO content, and origin of sulfur-rich magmas on Mercury. J. Geophys. Res., Planets 118, 138–146. https://doi.org/10.1029/2012JE004274.